

Single-Phase to Three-Phase Inverter with Small DC-Link Capacitor for Motor Drive System

ZHOU Yufei^{1*}, HUANG Wenxin²

1. College of Electronic and Information Engineering, Nanjing University of Aeronautics and Astronautics, Nanjing 211106, P. R. China;

2. College of Automation Engineering, Nanjing University of Aeronautics and Astronautics, Nanjing 211106, P. R. China

(Received 14 January 2019; revised 21 October 2019; accepted 9 December 2019)

Abstract: The electrolytic-capacitor-less (EL-cap-less) technique has been attracting more and more interests in these years. The EL-cap-less single-phase to three-phase inverter (STI) with front-end diode rectifier is applied to home electrical appliances. In EL-cap-less systems, film-type capacitor is used to suppress the high-frequency ripple components instead of smoothing the DC-link voltage. By using the EL-cap-less solution, reliability can be improved, lifetime can be increased and high power factor (PF) also can be realized. The EL-cap-less STI brings the opportunity to simplify system structure and lower cost. Because a certain DC-link capacitance is still required, the real PF is limited. To further improve the PF, the ripple components of current references are made in synchronous with the DC-link voltage. And the capacitance chosen guideline of the film-type capacitor also be presented. A prototype is built to verify its real performance.

Key words: AC-DC-AC converter; electrolytic-capacitor-less; high power factor

CLC number: TM46 **Document code:** A **Article ID:** 1005-1120(2019)06-0927-11

0 Introduction

As known to all, electronic equipments often suffer from high temperature for military and aviation applications. Thus electrolytic (EL) capacitors, whose lifetime greatly depends on the system temperature, are not preferable^[1-4]. And lifetime of a high-quality EL capacitor is typically 10 000 h at 105 °C. Many capacitor datasheets emphasize that lifetime would reduce by half if the core temperature of EL capacitor is increased to 105 °C. Meanwhile, in the field of commercial products, AC motors' drivers used in home electrical appliances are usually single-phase to three-phase inverters (STI) with front-end diode rectifier. The aluminum EL capacitors with large capacitance and low cost are often used in the DC-link in order to balance the instantaneous input and output power^[5-9]. However, they introduce some unwanted properties: (1) low power

density due to large volume occupied by EL capacitors; (2) low power factor (PF) and requiring an additional power factor correction (PFC) circuit^[10-11], or a large inductance reactor^[12-13] in front of DC-link, which increases the volume and declines the efficiency; and (3) low reliability due to finite lifetime and high failure rate of EL capacitors^[2,14].

In order to save energy, improve reliability and further extend lifetime of the motor drive system, many researches have been studied and reported^[15-21]. Topology of the EL-cap-less STI is shown in Fig.1. With film capacitors in the DC-link instead of large EL capacitors, some advantages stand out:

(1) Decreasing circuit elements and reducing system volume and weight, leading to improved power density and higher power integration potential;

(2) Improving circuit reliability and extending life time of the drive system by avoiding the use of high failure rate EL capacitors;

*Corresponding author, E-mail address: zhoyf@nuaa.edu.cn.

How to cite this article: ZHOU Yufei, HUANG Wenxin. Single-Phase to Three-Phase Inverter with Small DC-Link Capacitor for Motor Drive System[J]. Transactions of Nanjing University of Aeronautics and Astronautics, 2019, 36(6):927-937. <http://dx.doi.org/10.16356/j.1005-1120.2019.06.006>

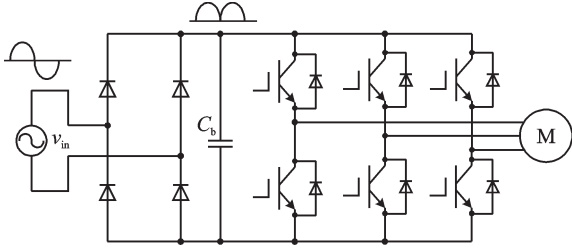


Fig.1 Topology of the EL-cap-less STI with front-end diode rectifier

(3) PF can be improved by some proposed control method^[6-8,18-20].

Whereas, some disadvantages also exist: DC-link voltage contains large ripple, leading to lower voltage utilization, larger speed ripple and slower dynamic response; energy cannot feedback to the input source owing to the front-end diode rectifier, making it not suitable for applications requiring rapid load variation or braking. These characteristics limit its applications but donot hinder the possible using in some variable-frequency AC motor drivers for home electrical appliances, such as compressor of air conditioner, since neither the rapid dynamic response nor the braking is needed in these systems. Therefore, it has the chance to replace EL capacitors with film-type capacitors.

The goal of this paper is to present capacitance chosen guideline of the film-type DC-link capacitor and harmonics injection method of STI with front-end diode rectifier, so that film-type capacitors can be employed to achieve a longer lifetime and higher system integration for motor drive system. Power factor calculation and DC-link capacitor estimation of STI with front-end diode rectifier are described in Section II. Control method of EL-cap-less STI based motor drive system is described in Section III. Finally, simulation and experimental results are included in Section IV.

1 Film-Type Capacitor of STI with Front-End Diode Rectifier

1.1 Input power factor calculation

Fig.2(a) shows the envelope lines of input voltage v_{in} , DC-link voltage v_b and input current i_{in} for EL-cap-less STI. Due to a small amount of capaci-

tance still exists, the valley of DC-link voltage is V_{bm} rather than zero. During the intervals of $[0, (\pi - \theta)/2)$ and $((\pi + \theta)/2, \pi]$ (θ is the conduction width of diode rectifier), DC-link voltage reaches V_{bm} , so input current $i_{in}=0$. During the interval of $[(\pi - \theta)/2, (\pi + \theta)/2]$, input current i_{in} changes in a sinusoidal way. Therefore, input AC voltage and current across the line cycle can be expressed as

$$v_{in}(t) = V_m \sin \omega_{in} t$$

$$i_{in}(t) = \begin{cases} I_m \sin \omega_{in} t & \frac{\pi - \theta}{2} \leq \omega_{in} t \leq \frac{\pi + \theta}{2} \\ 0 & 0 \leq \omega_{in} t < \frac{\pi - \theta}{2} \text{ or} \\ & \frac{\pi + \theta}{2} < \omega_{in} t \leq \pi \end{cases} \quad (1)$$

where V_m and I_m are the magnitude of input voltage and current, and ω_{in} is the angular frequency of AC source, respectively. The input active power is derived as

$$P_{ina} = \frac{1}{\pi} \int_{\frac{\pi - \theta}{2}}^{\frac{\pi + \theta}{2}} V_m \sin(\omega_{in} t) I_m \sin(\omega_{in} t) dt = \frac{V_m I_m (\theta + \sin \theta)}{2\pi} \quad (2)$$

The RMS of input current can be expressed as

$$I_{inrms} = \sqrt{\frac{1}{\pi} \int_{\frac{\pi - \theta}{2}}^{\frac{\pi + \theta}{2}} (I_m \sin \omega_{in} t)^2 dt} = I_m \sqrt{\frac{\theta + \sin \theta}{2\pi}} \quad (3)$$

Then the apparent power S can be derived as

$$S = \frac{V_m}{\sqrt{2}} I_{inrms} = \frac{V_m I_m}{2} \sqrt{\frac{\theta + \sin \theta}{\pi}} \quad (4)$$

PF can be calculated as

$$PF = \frac{P_{ina}}{S} = \sqrt{\frac{\theta + \sin \theta}{\pi}} \quad (5)$$

From the geometrical view of Fig.2(a), relationship between valley and peak of v_b can be derived as

$$\cos \frac{\theta}{2} = \frac{V_{bm}}{V_{bM}} = k_b \quad (6)$$

where k_b is the valley-to-peak ratio of DC-link voltage. From Eqs.(5) and (6), the relationship between PF and k_b is shown in Fig.2(b), where k_b is obviously related to PF. From Fig.2(b), the power factor is higher than 0.9 when $k_b \leq 0.7$.

The DC-link valley voltage can be reduced and the conduction width θ of the input current i_{in} can be enlarged by using smaller DC-link capacitor, and

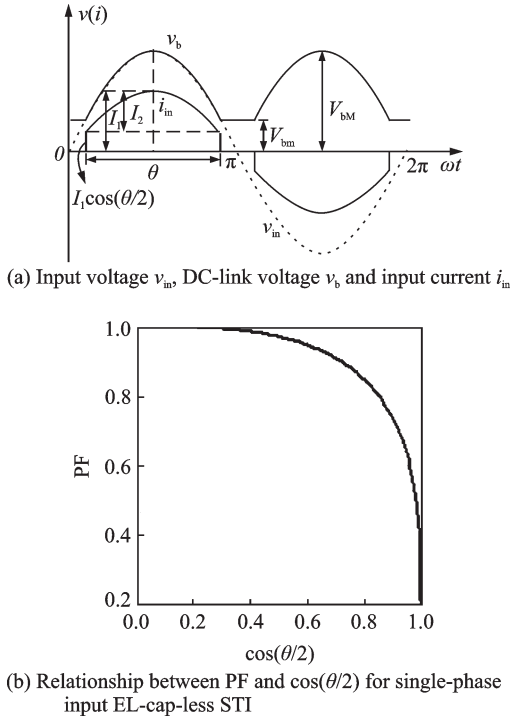


Fig.2 Relationship among voltages and currents, and relationship between PF and $\cos(\theta/2)$

therefore make i_{in} more sinusoidal and increase the PF. However, a certain amount of capacitance is still required to storage energy in the real system. This is because motor speed should be maintained during the DC-link valley voltage due to the moment of inertia, which induces the motor to run in the generation mode. The energy feedback to the DC-link should be smoothed during the DC-link valley voltage to prevent overshoot. The EL-cap-less STI is suitable for low and medium power application with slow speed dynamic response, especially for load with larger moment of inertia.

1.2 DC-link capacitance estimation

Assuming that the PF is of unity, the instantaneous input current can be expressed as

$$i_{in}(t) = I_m \sin(\omega_{in}t) \quad (7)$$

Then the instantaneous input power can be derived as

$$p_{in}(t) = \frac{V_m I_m}{2} [1 - \cos(2\omega_{in}t)] \quad (8)$$

The average input power can be derived as

$$P_{inave} = \frac{V_m I_m}{2} \quad (9)$$

To control the PF to be high, output power unavoidably coupled with ripple components synchro-

nous with line frequency. Supposing efficiency of the inverter is 100%, the input power of the inverter is equal to the apparent power of the motor

$$p_{inv}(t) = p_M(t) = p_R(t) + p_L(t) + p_{em}(t) \quad (10)$$

where the apparent power p_M of the permanent magnet synchronous motor (PMSM) includes three parts: the dissipative power of stator resistance p_R , the charge and discharge power of stator inductance p_L and the electromagnetic power p_{em} , where $p_R(t) = \frac{3}{2} R_s [i_d(t)^2 + i_q(t)^2]$, $p_L(t) = \frac{3}{2} \left[L_d \frac{di_d(t)}{dt} i_d(t) + L_q \frac{di_q(t)}{dt} i_q(t) \right]$, $p_{em}(t) = \frac{3}{2} \omega_e [\Psi_f i_q(t) + (L_d - L_q) i_d(t) i_q(t)]$, separately, in which ω_e is the angular speed of rotor, Ψ_f is the rotor linkage flux, L_d and L_q are d -axis and q -axis inductances, i_d and i_q are d -axis and q -axis rotor currents, and R_s is the stator resistance. Apparently, d -axis and q -axis rotor currents include ripple components fluctuating with twice line frequency. Therefore, $p_R(t)$, $p_L(t)$ and $p_{em}(t)$ are all synchronous with twice line frequency. Because the value of R_s , L_d and L_q are relatively small, the variation of $p_R(t)$ and $p_L(t)$ can be neglected. The apparent power of PMSM can be expressed as

$$p_M(t) = \frac{3}{2} [v_d(t) i_d(t) + v_q(t) i_q(t)] \quad (11)$$

The voltage equations of PMSM can be expressed as

$$\begin{bmatrix} v_d(t) \\ v_q(t) \end{bmatrix} = \begin{bmatrix} R_s + pL_d & -\omega_e L_q \\ \omega_e L_d & R_s + pL_q \end{bmatrix} \begin{bmatrix} i_d(t) \\ i_q(t) \end{bmatrix} + \begin{bmatrix} 0 \\ \omega_e \Psi_f \end{bmatrix} \quad (12)$$

where p is the differential operator. The power flows through DC-link capacitor C_b is

$$p_c(t) = v_c(t) i_c(t) = \omega_{in} C_b V_m^2 \sin(2\omega_{in}t) \quad (13)$$

Here, $p_c(t)$ is determined by capacitance and amplitude of the input voltage, as indicated in Eq.(13). Key waveforms of the EL-cap-less STI when the PF is of unity are shown in Fig.3(a). When $p_{in}(t) > p_{inv}(t)$, $p_c(t) > 0$, and $v_c(t)$ increases, C_b is charged; when $p_{in}(t) < p_{inv}(t)$, $p_c(t) < 0$, and $v_c(t)$ decreases, C_b is discharged.

The energy charging C_b from 0 to $\pi/2$ is

$$\Delta E = \int_0^{\frac{\pi}{2}} p_c(t) dt = \frac{C_b V_m^2 \omega_{in}}{2} \quad (14)$$

With Eqs. (8) and (10), ΔE also can be expressed as

$$\Delta E = \int_0^{\frac{\pi}{2}} [p_m(t) - p_{inv}(t)] dt \quad (15)$$

From Eqs.(14) and (15), we can estimate DC-link capacitance. To simplify the calculation further, $p_R(t)$ and $p_L(t)$ can be neglected because of much smaller effect of $p_R(t)$ and $p_L(t)$ compared with $p_{em}(t)$. Then the input power of inverter equals to the electromagnetic power of the motor $p_{em}(t)$. Because the inverter controller regulates the speed of the PMSM motor to be smooth, the ripple components of the motor torque exists. Then $p_{inv}(t)$ can be derived as

$$p_{inv}(t) = T_m \omega_m \sin(\omega_m t)^2 \quad (16)$$

While the average value of $p_{inv}(t)$ can be derived as

$$P_{inv} = \frac{T_m \omega_m}{2} \quad (17)$$

where T_m is the magnitude of torque, and ω_m the mechanical angular frequency. Supposing that the efficiency of inverter is 100%, the average power of input source P_{inave} is equal to the average input power of inverter P_{inv} and also output power P_o . Then peak value of torque T_m can be expressed as

$$T_m = \frac{2P_o(\theta + \sin\theta)}{\pi\omega_m} \quad (18)$$

From Eq.(18), the magnitude of torque is related to the conduction width θ . The larger θ would lead to higher PF and T_m further.

From Eqs. (14), (15) and (16), we have

$$C_b = \frac{\pi(V_m I_m - \omega_m T_m)}{2V_m^2 \omega_{in}} \quad (19)$$

Relationship between T_m , C_b and the conduction width θ can be illustrated by taking an EL-cap-less STI as an example. The output power $P_o=500$ W, the magnitude and frequency of input voltage is 311 V and 50 Hz. From Fig.2(b), the relationship between PF and k_b can be found, that is $PF \geq 0.9$, when $k_b \leq 0.7$. So substituting Eq. (6) into Eq. (18) yields

$$T_m = \frac{2P_o \{ 2 \arccos(k_b) + \sin [2 \arccos(k_b)] \}}{\pi\omega_m} \quad (20)$$

Then curves of T_m as a function of ω_m can be

shown in Fig.3(b). When ω_m is about 1 000 rad/s and $k_b=0.7$, the peak value of torque T_m is about 0.8 N•s. If k_b is reduced to 0.3 and PF is about 0.99, T_m is about 1 Ns. The torque ripple is larger when PF is improved. From Eq. (19), curves of C_b as a function of k_b can be shown in Fig.3(c). When $k_b=0.7$, C_b is about 10 μ F. The higher PF is, the smaller C_b is needed to maintain the conduction width of the diode rectifier.

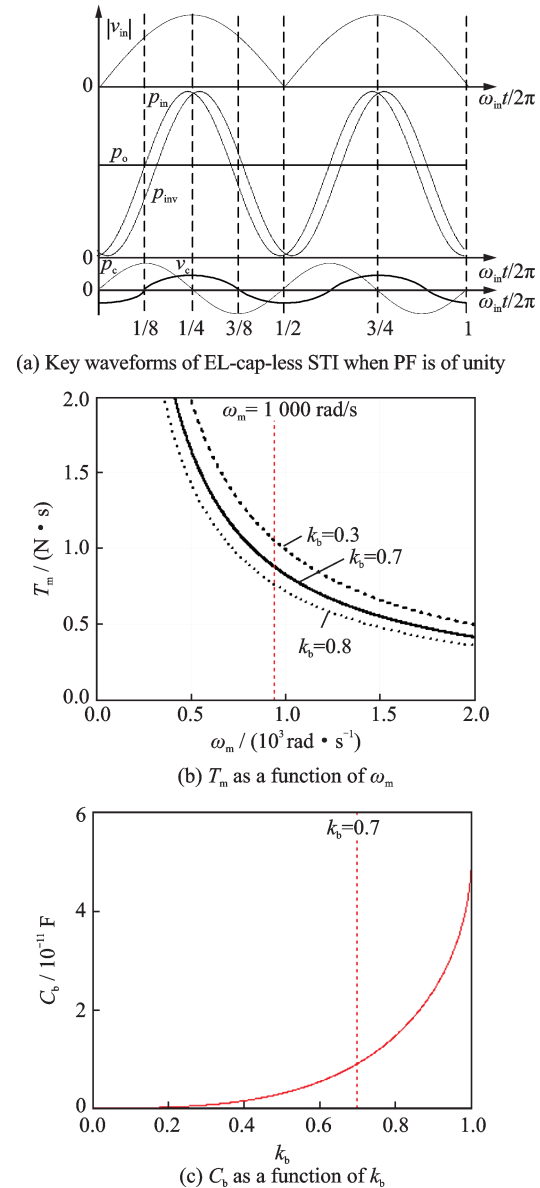


Fig.3 Key waveforms of EL-cap-less STI; and T_m as a function of ω_m ; and C_b as a function of k_b

2 Control Method of EL-Cap-Less STI Based Motor Drive System

The overall control block diagram of EL-cap-

less STI is shown in Fig.4. The control method is a modified vector control suitable for EL-cap-less STI with improved PF. The speed controller output is the amplitude reference of q -axis current. The ripple components of d -axis and q -axis current reference are made in synchronous with the DC-link voltage to improve the PF. In addition, the real minimum value of the DC-link voltage is low when the desired PF is high as indicated in Fig.2(a). The voltage lim-

iter is necessary for preventing over modulation. When the DC-link voltage varies during every line period, both d -axis and q -axis voltage which are the outputs of current loops cannot change rapidly due to the feedback control. Therefore, a voltage feed-forward factor should be introduced into the current loops, to improve speed response of the feedback control during over-modulation correction and also prevent large errors of v'_d , v'_q and v_d , v_q further.

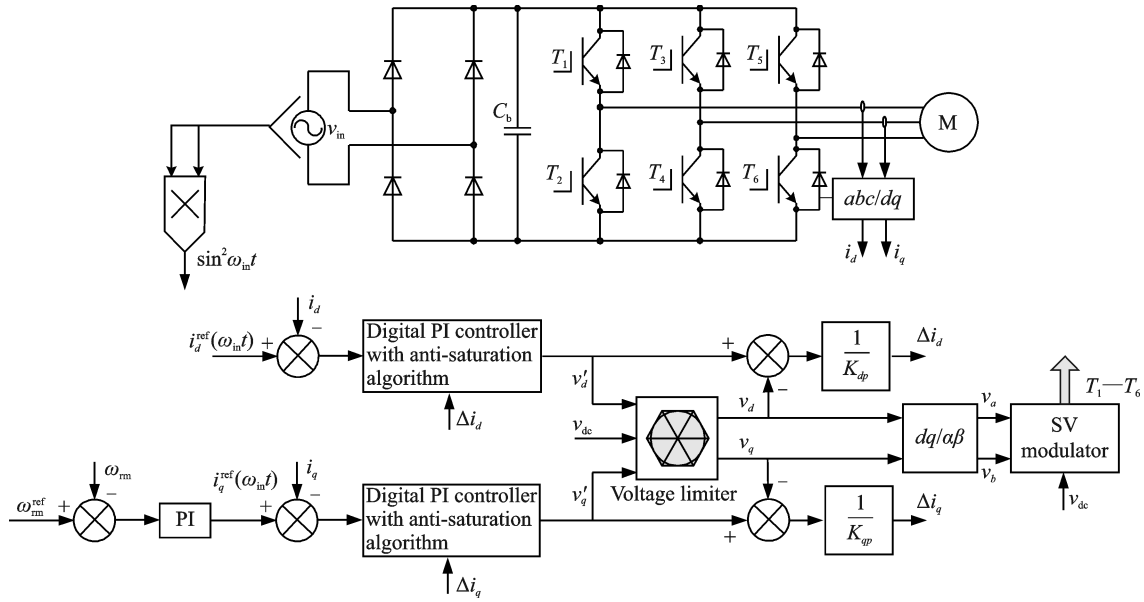


Fig.4 Overall control block diagram of EL-cap-less STI system

2.1 The d -axis current controller

For the motor drive system, the flux-weakening-control method is applied in order to maintain the motor speed after DC-link voltage reaches its minimum value. According to the voltage constraint ellipse, d -axis current reference i_d^{ref} can be expressed as

$$i_d^{\text{ref}} = -\frac{\psi_f}{L_d} + \frac{1}{L_d} \sqrt{\left(\frac{v_{dc}}{\sqrt{3}\omega_e}\right)^2 - (L_q i_q)^2} \quad (21)$$

However, Eq.(21) is not suitable for the EL-cap-less STI PMSM drive system^[18]. As mentioned above, d -axis and q -axis rotor currents are fluctuating. Therefore, the voltage constraint ellipse cannot be derived and the traditional flux-weakening-control method is not appropriate here. Because the DC-link voltage couples with twice line frequency component, the effective voltage level is lower than that

of constant voltage if keeping the same peak value. That means to reach the same required speed value, more d -axis flux-weakening current should be applied. And the i_d^{ref} fluctuation caused by DC-link voltage would aggravate the current regulation performance^[18]. i_d^{ref} should be expressed as follow in this system.

$$i_d^{\text{ref}}(t) = I_{\text{dofs}} + I_{\text{ripple}} \cdot \sin(2\omega_{in}t + \delta) \quad (22)$$

where I_{dofs} is a negative offset component, I_{ripple} the magnitude of the harmonic component, and δ the deviation angle between input voltage and the harmonic component. These parameters are manually regulated to obtain high power factor under different operation conditions.

2.2 The q -axis current controller

To obtain high PF, the DC-link voltage valley should be as low as possible. Low DC-link voltage valley would enlarge the conduction width of front-

end diode rectifier and improve the input current quality. So the desirable polarity of q -axis current should be positive to prevent power feed back to the dc link, and this is realized by setting minimum value of q -axis current reference to zero. Though the controlled polarity of q -axis current reference is positive, the real q -axis current is slightly negative. This is caused by the electromotive force which would rise up the DC-link voltage valley under steady state. The q -axis current reference is given as

$$i_q^{\text{ref}}(t) = I_q \cdot \sin^2(\omega_{\text{in}}t + \lambda) \quad (23)$$

where I_q is the output of the speed regulator, and λ the deviation angle between input voltage and the ripple component. And λ is manually tuned to obtain high PF under different operation conditions.

2.3 Phase angle testing of input voltage

As mentioned above, the d -axis and q -axis current references have ripple components which are both synchronous with the input voltage. Therefore, phase angle of the input voltage should be obtained first.

For single-phase converter, coordinate transformation cannot be performed directly. It is necessary to reconstruct the coordinate transformation in single-phase input system.

Supposing that the arbitrary input voltage expression is as follow

$$v_{\text{in}}(t) = V_m \sin(\omega_{\text{in}}t + \psi) \quad (24)$$

where ψ is the initial phase angle of the input voltage. Eq. (24) can be resolved into

$$v_{\text{in}}(t) = V_{d\text{in}} \cdot \sin(\omega_{\text{in}}t) + V_{q\text{in}} \cdot \cos(\omega_{\text{in}}t) \quad (25)$$

where $V_{d\text{in}} = V_m \cdot \cos\psi$ and $V_{q\text{in}} = V_m \cdot \sin\psi$. The variation of $V_{d\text{in}}$ and $V_{q\text{in}}$ is small, so $V_{d\text{in}}$ and $V_{q\text{in}}$ can be treated as the dc component. A decoupling method is presented to decouple the dc component from Eq.(25). The control block diagram is shown in Fig.5, in which a low-pass filter is used to filter out the harmonics at the switching frequency first.

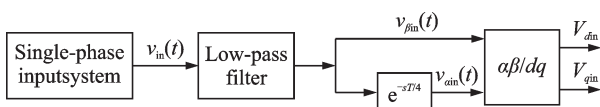


Fig.5 The d - q decoupling control block diagram in virtual stationary coordinate

Then a virtual two phase stationary coordinate is constructed by delaying 1/4 period of the actual input AC voltage. Finally, $V_{d\text{in}}$ and $V_{q\text{in}}$ can be obtained from park transformation^[22-23].

The orthogonal signal which delaying 1/4 period of the actual input AC voltage can be expressed as

$$v'_{\text{in}}(t) = V_m \cdot \sin\left(\omega_{\text{in}}t + \psi + \frac{\pi}{2}\right) = V_m \cdot \cos(\omega_{\text{in}}t + \psi) \quad (26)$$

Then $\{v_{\text{in}}(t), v'_{\text{in}}(t)\}$ constructs two-phase virtual orthogonal coordinate, $\alpha\beta$ coordinate. And $v_{\alpha}(t)$ and $v_{\beta}(t)$ can be defined as

$$\begin{bmatrix} v_{\alpha}(t) \\ v_{\beta}(t) \end{bmatrix} = \begin{bmatrix} v_{\text{in}}(t) \\ v'_{\text{in}}(t) \end{bmatrix} = \begin{bmatrix} V_m \cdot \cos(\omega_{\text{in}}t + \psi) \\ V_m \cdot \sin(\omega_{\text{in}}t + \psi) \end{bmatrix} \quad (27)$$

$V_{d\text{in}}$ and $V_{q\text{in}}$ can be obtained by $\alpha\beta$ - dq coordinate transformation module to transform the AC voltages into DC values

$$\begin{bmatrix} V_{d\text{in}} \\ V_{q\text{in}} \end{bmatrix} = \begin{bmatrix} \cos(\omega_{\text{in}}t) & \sin(\omega_{\text{in}}t) \\ -\sin(\omega_{\text{in}}t) & \cos(\omega_{\text{in}}t) \end{bmatrix} \begin{bmatrix} v_{\alpha}(t) \\ v_{\beta}(t) \end{bmatrix} = V_m \begin{bmatrix} \cos\psi \\ \sin\psi \end{bmatrix} \quad (28)$$

Then the initial phase angle of the input voltage can be obtained as

$$\psi = \arctan \frac{V_{q\text{in}}}{V_{d\text{in}}} \quad (29)$$

The amplitude of the input voltage can also be obtained as

$$V_m = \sqrt{V_{d\text{in}}^2 + V_{q\text{in}}^2} \quad (30)$$

2.4 Anti-saturation current control loop

In the traditional vector control, the d -axis and q -axis current references are of constant DC values. Therefore, only two PI regulators are applied to the current controller to realize precise tracking of d -axis and q -axis current references. The outputs of the current controller, v_d and v_q , are limited by the voltage limiter to prevent over-modulation, and then input to the inverse park transformation block to generate driving signal of PMSM motor. The traditional current control block diagram is shown in Fig.6(a).

Different from traditional vector control, the d -axis and q -axis currents are rippled with twice line

frequency. This kind of current would lead to output saturation of the current PI controller if traditional current control method is used, and result in large harmonic components of the input AC current. The robust EL-cap-less STI drive system must prevent the output saturation of the current control loop. The anti-saturation current control block diagram is shown in Fig.6(b). The algorithm is based on the feedback control of saturation variables Δi_d and Δi_q . When the outputs of the current controller v'_d, v'_q are saturated, they are calculated again with outputs of the voltage limiter v_d^{lim} and v_q^{lim} , which can be expressed as

$$v_d = \begin{cases} v'_d & v'_d \leq v_d^{lim} \\ \text{sgn}(v'_d) v_d^{lim} & v'_d > v_d^{lim} \end{cases} \quad (31)$$

$$v_q = \begin{cases} v'_q & v'_q \leq v_q^{lim} \\ \text{sgn}(v'_q) v_q^{lim} & v'_q > v_q^{lim} \end{cases}$$

The integrators are corrected by the feedback of Δi_d and Δi_q within one sampling period, leading to rapid regulation. In next sampling period, the output of the current controller has already been corrected, so the anti-saturation current tracking control is achieved in one current sampling period and the input AC current waveform can be improved.

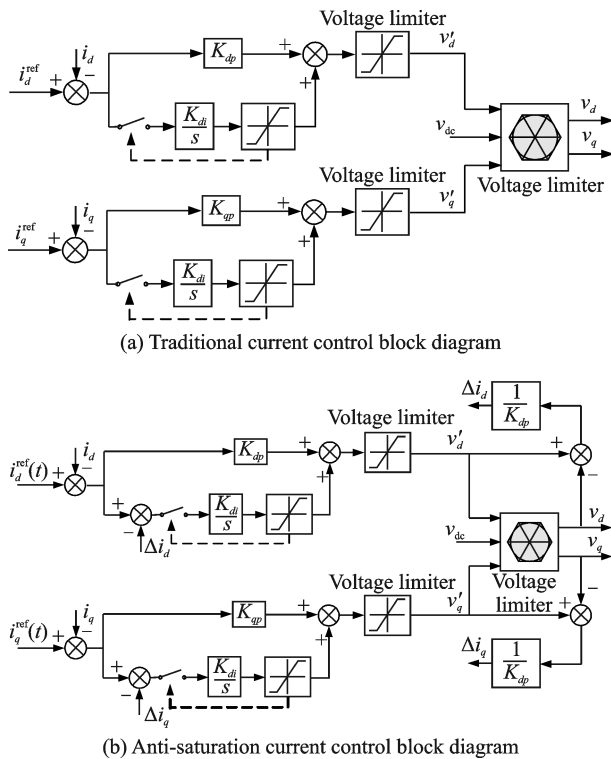


Fig.6 Current control block diagram

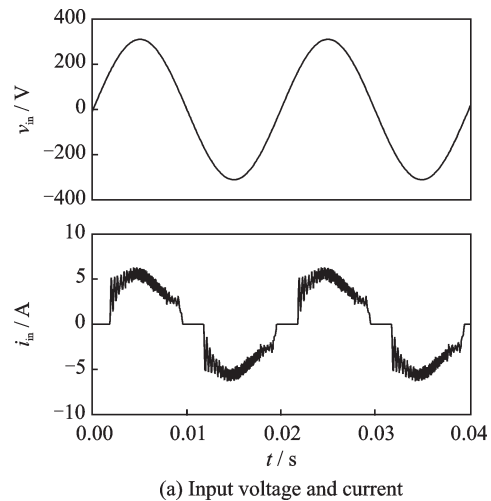
3 Simulation and Experimental Results

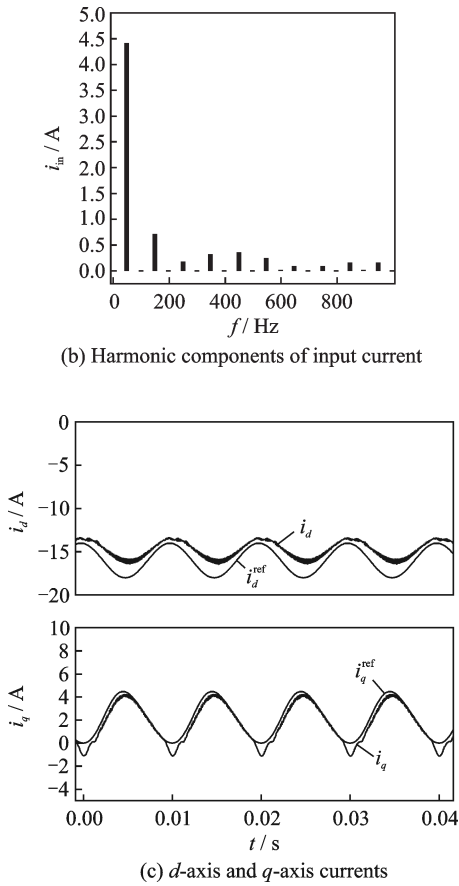
3.1 Simulation results

A simulation model of EL-cap-less STI has been constructed by using PLECS software. The dc-link capacitor C_b is about 15 μF . The motor parameters of PMSM are listed below:

- (1) Stator winding resistance r_1 : 0.495 Ω ;
- (2) Stator d -axis inductance L_d : 5.46 mH, q -axis inductance L_q : 12.06 mH;
- (3) Permanent magnet flux linkage Ψ : 0.138 6 Wb;
- (4) Inertia J : 9.6×10^{-4} $\text{kg} \cdot \text{m}^2$;
- (5) Pole number: 6.

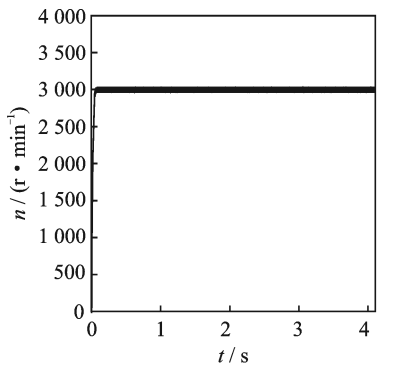
Fig.7 shows the simulation waveforms under motor speed of 3 000 r/min. Fig.7(a) shows the input voltage and current, from which i_m is almost in the same phase with v_m , and conduction width is about 120° . Fig.7(b) shows harmonic components of i_m . The amplitude of 3rd, 5th, 7th and 9th harmonic components are 0.7, 0.165, 0.3 and 0.34 A, separately. Fig.7(c) shows waveforms of d -axis and q -axis current. The current control loop with anti-saturation algorithm can realize rapid tracking of the current reference injected with large ripple. The anti-saturation algorithm corrects the output variables of current controller during the current sampling period, in the form of feed-forward saturation variables Δi_d and Δi_q . Fig.7(d) shows the waveform of the motor speed with its reference of 3 000 r/min. The





(b) Harmonic components of input current

(c) *d*-axis and *q*-axis currents



(d) Motor speed response to step reference

Fig.7 Simulation waveforms

speed ripple is very small, and the start-up is quick and without oscillation.

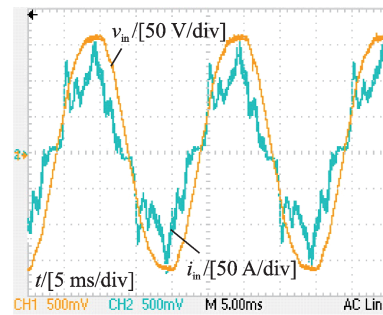
3.2 Experimental results

To verify the validity of the proposed methods, an EL-cap-less STI prototype, is constructed. The power devices and components of the EL-cap-less STI are listed as follows:

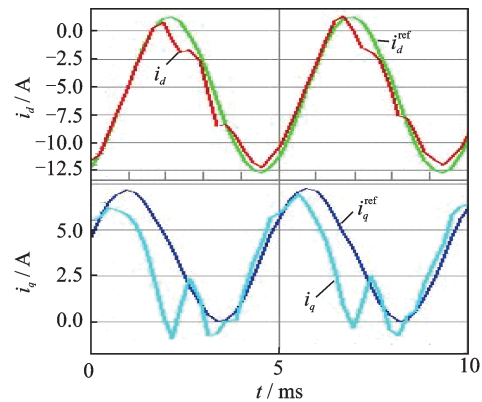
- (1) DC-link capacitor: 15 μ F metalized polypropylene film capacitor;
- (2) Power devices: IPM module PS21A79.

Fig.8 shows key experimental waveforms with

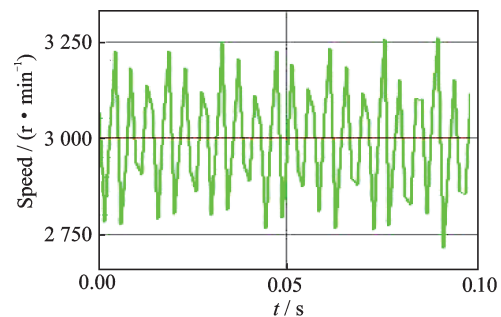
an air conditioning compressor as the load. The motor parameters of the tested PMSM are the same as those in the simulation part. The input AC voltage is set to 220 V_{rms}/50 Hz. The switching frequency is 10 kHz. Figs. 8 (a) — (h) show experimental waveforms under motor speed of 3 000 r/min and 6 000 r/min. Figs.8(a) and (e) show waveforms of input AC voltage and current, where i_m is almost in the same phase with v_m , while the sinusoidal waveform is not good enough and has harmonic components. The tested PF is 0.95 and can meet the relative standard. The PF is improved to 0.98 under 6 000 r/min. In case of film-type DC-link capacitor system, especially in single phase system, it is hard to achieve the satisfactory of the current regulation



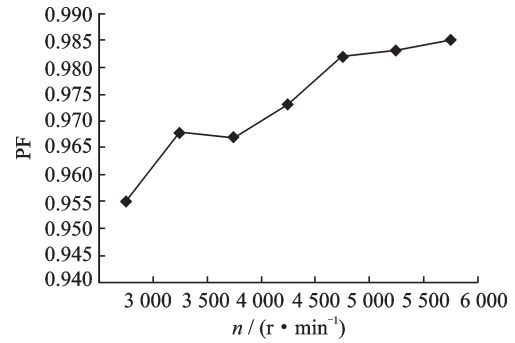
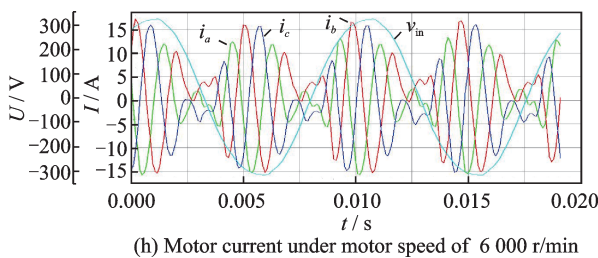
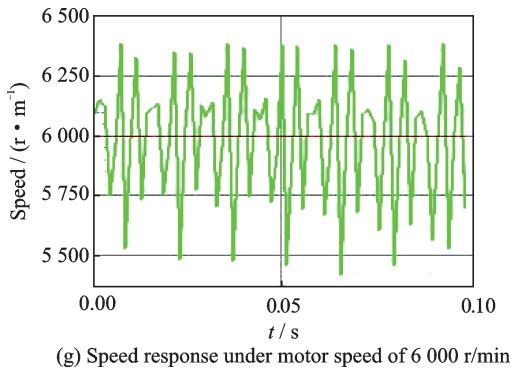
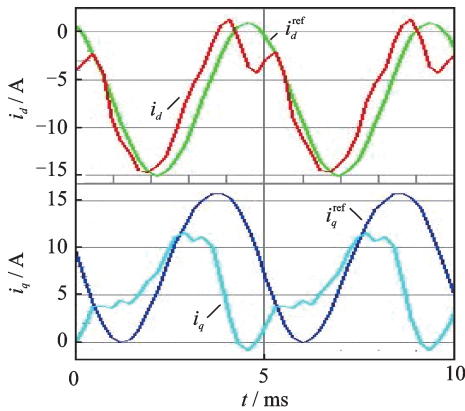
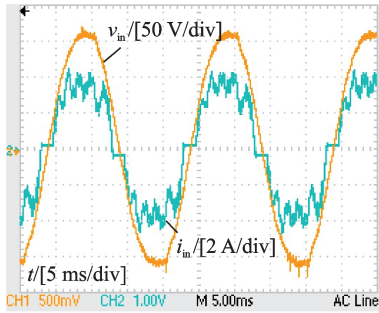
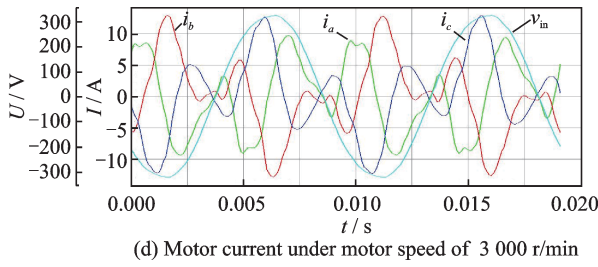
(a) Input AC voltage and current under motor speed of 3 000 r/min



(b) *d*-axis and *q*-axis current under motor speed of 3 000 r/min



(c) Speed response under motor speed of 3 000 r/min



(i) PF comparison under different motor speeds

Fig.8 Experimental results

performance because of lack of voltage margin and digital delays. Figs.8(b) and (f) show experimental waveforms of d - and q -axis current. Larger negative d -axis current reference for flux-weakening is applied in order to raise the motor speed. The q -axis current reference is a fluctuating waveform formed by the output of speed regulator and the grid phase angle. Figs. 8 (c) and (g) show the experimental waveform of the speed response, whose errors are lower than $\pm 9\%$. The motor currents are shown in Figs.8(d) and (h), whose envelope is synchronized with the input AC voltage. Fig.8(i) presents the input power factor comparison under different input power. The PF value increases as the input power increases, and reaches its highest value under motor speed of 6 000 r/min. Table 1 shows the comparison results of harmonics and standard IEC61000-3-2 Class A of input current under different motor speeds. Therefore, the ripple components of input current can meet the standard. The efficiency of EL-cap-less STI system is 85.6% at the rated speed of 6 000 r/min, and that of the structure shown in Fig.1 with aluminum electrolytic capacitor is 89% under the same condition.

4 Conclusions

This paper proposes an EL-cap-less STI system featured with simple structure, improved reliability and high PF. In the system, the DC-link storage capacitance can be significantly reduced so that film-type capacitors can be used instead of electrolytic capacitors. The capacitance choosing guideline of the film-type capacitor is presented. To achieve high PF, harmonics synchronized with the DC-link volt-

Table 1 Harmonics v.s. standard IEC61000-3-2 Class A under different motor speed

Odd harmonic order	Real value I_m/A		Requirement (IEC61000-3-2)/A
	Case 1 3 000 r/min	Case 2 6 000 r/min	
1	1.152	3.159	
3	0.278	0.438	2.300
5	0.156	0.313	1.140
7	0.098	0.227	0.770
9	0.070	0.143	0.400
Even harmonic order	Real value I_m/A		Requirement (IEC61000-3-2)/A
	Case 1 3 000 r/min	Case 2 6 000 r/min	
2	0.005	0.014	1.080
4	0.005	0.006	0.430
6	0.006	0.003	0.300
8	0.006	0.002	0.230
10	0.003	0.004	0.184

age are injected into the d - and q -axis current controllers. To prevent saturation of the current controller output, anti-saturation current tracking control is employed. Simulation model and laboratory prototype are built, and steady-state performances are tested to show its validity.

References

- [1] WANG S, RUAN X B, YAO K, et al. A flicker-free electrolytic capacitor-less AC-DC LED driver[J]. IEEE Transactions on Power Electronics, 2012, 27(11): 4540-4548.
- [2] AMARAL A M R, CARDOSO A J M. On-line fault detection of aluminum electrolytic capacitors, in step-down DC-DC converters, using input current and output voltage ripple[J]. IET Power Electronics, 2012, 5(3): 315-322.
- [3] VOGELSBERGER M A, WIESINGER T, ERTL H. Life-cycle monitoring and voltage-managing unit for DC-link electrolytic capacitors in PWM converters[J]. IEEE Transactions on Power Electronics, 2012, 26(2): 493-503.
- [4] BOTH J. The modern era of aluminum electrolytic capacitors[J]. IEEE Electrical Insulation Magazine, 2015, 31(4): 24-34.
- [5] KHAJEHODDIN S A, GHARTEMANI M K, JAIN P K, et al. DC-bus design and control for a single-phase grid-connected renewable converter with a small energy storage component[J]. IEEE Transactions on Power Electronics, 2013, 28(7): 3245-3254.
- [6] INAZUMA K, OHISHI K, HAGA H. High-power-factor control for inverter output power of IPM motor driven by inverter system without electrolytic capacitor[C]// IEEE Proceedings of ISIE. [S.l.]: IEEE, 2011: 619-624.
- [7] HAGA H, NISHIYA K, KONDO S, et al. High power factor control of electrolytic capacitor less current-fed single-phase to three-phase power converter[C]//IEEE Proceedings of IPEC. [S.l.]: IEEE, 2011: 443-448.
- [8] INAZUMA K, UTSUGI H, OHISHI K, et al. High power factor single-phase diode rectifier driven by repetitive controlled IPM motor[J]. IEEE Transactions on Industrial Electronics, 2013, 60(10): 4427-4437.
- [9] RIBEIRO H S, BORGES B V. High-performance voltage-fed AC-DC full-bridge single-stage power factor correctors with a reduced DC bus capacitor[J]. IEEE Transactions on Power Electronics, 2014, 29(6): 2680-2692.
- [10] BHIM S, SANJEEV S, AMBRISH C, et al. Comprehensive study of single-phase AC-AC power factor corrected converters with high-frequency isolation[J]. IEEE Transactions on Industrial Informatics, 2011, 7(4): 540-555.
- [11] MEHDI N, GERRY M. A new single-phase single-stage three-level power-factor-correction AC-AC converter with phase-shift modulation[J]. IEEE Transactions on Industry Applications, 2013, 60(9): 3731-3735.
- [12] JOVANOVIĆ M M, JANG Y. State-of-the-art, single-phase, active power-factor-correction techniques for high-power applications-An overview[J]. IEEE Transactions on Industrial Electronics, 2005, 52(3): 701-708.
- [13] RAJESH M, SINGH B. Analysis, design and control of single-phase three-level power factor correction rectifier fed switched reluctance motor drive[J]. IET Power Electronics, 2014, 7(6): 1499-1508.
- [14] BRAHAM A, LAHYANI A, VENET P, et al. Recent developments in fault detection and power loss estimation of electrolytic capacitors[J]. IEEE Transactions on Power Electronics, 2010, 25(1): 33-43.
- [15] SUN M X, HUANG W Q, WANG Y, et al. Experiment on a double-foot stepping piezoelectric linear motor[J]. Transactions of Nanjing University of Aeronautics and Astronautics, 2018, 35(3): 423-431.
- [16] LEE W J, SUL S K. DC-Link Voltage stabilization for reduced DC-link capacitor inverter[J]. IEEE Transactions on Industry Application, 2014, 50(1):

- 404-414.
- [17] SUPPHARANGSAN W, WANG J B. Switching technique for minimization of DC-link capacitance in switched reluctance machine drives[J]. *IET Electrical Systems in Transportation*, 2015, 5(4): 185-193.
- [18] JUNG H S, CHEE S J, SUL S K, et al. Control of three-phase inverter for AC motor drive with small dc-link capacitor fed by single-phase AC source[J]. *IEEE Transactions on Industry Application*, 2014, 50(2): 1074-1081.
- [19] SON Y, HA J I. Direct power control of a three-phase inverter for grid input current shaping of a single-phase diode rectifier with a small dc-link capacitor [J]. *IEEE Transactions on Power Electronics*, 2015, 30(7): 3794-3803.
- [20] SON Y, HA J I. Discontinuous grid current control of motor drive system with single-phase diode rectifier and small dc-link capacitor[J]. *IEEE Transactions on Power Electronics*, 2017, 32(2): 1324-1334.
- [21] YU X Q, JIANG B, ZHANG K. Sensor micro fault diagnosis and the application on motors[J]. *Journal of Nanjing University of Aeronautics and Astronautics*, 2018, 50(3): 321-328. (in Chinese)
- [22] MONFARED M, GOLESTAN S, GUERRERO J M. Analysis, design, and experimental verification of a synchronous reference frame voltage control for single-phase inverters[J]. *IEEE Transactions on Industrial Electronics*, 2014, 61(1): 258-269.
- [23] GU Y J, WANG Y X, XIANG X, et al. Improved virtual vector control of single-phase inverter based on unified model [J]. *IEEE Transactions on Energy Conversion*, 2014, 29(3): 611-618.
- Acknowledgements** This work was supported by the Fundamental Research Funds for the Central Universities (No. NT2018011), and the China Postdoctoral Science Foundation (No. 2015M580424).
- Authors** Dr. ZHOU Yufei received the B.S., M.S. and Ph.D. degrees from the Nanjing University of Aeronautics and Astronautics (NUAA), Nanjing, China, in 2006, 2009 and 2013, respectively. She joined in Nanjing University of Aeronautics and Astronautics in 2013, where she is an assistant professor. Her current research interests are renewable energy generation and integrated power electronics modules. Prof. HUANG Wenxin received the B.S. degree from Southeast University, Nanjing, China, in 1988, and the M.S. and Ph.D. degrees from the Nanjing University of Aeronautics and Astronautics (NUAA), Nanjing, in 1994 and 2002, respectively. In 2003, he joined the College of Automation Engineering, NUAA, where he is currently a Professor. His current research interests include design and control for electrical machine systems and renewable energy generation.
- Author contributions** Dr. ZHOU Yufei designed the study, compiled the models, conducted the analysis, interpreted the results and wrote the manuscript. Prof. HUANG Wenxin contributed to the discussion and background of the study.
- Competing interests** The authors declare no competing interests.

(Production Editor: Zhang Huangqun)